Influence of pre-impact shape of an oil droplet on the post-impact flow dynamics at air-water interface

Joydip Chaudhuri,[1] Tapas Kumar Mandal,[1, 2, 3] and Dipankar Bandyopadhyay[1, 2, 3, *]

[1] *Department of Chemical Engineering, Indian Institute of Technology Guwahati, Assam 781039, India*
[2] *Centre for Nanotechnology, Indian Institute of Technology Guwahati, Assam 781039, India*
[3] *School of Health Sciences and Technology, Indian Institute of Technology Guwahati, Assam 781039, India*

(Dated: May 13, 2022)

I. ELECTRONIC SUPPORTING INFORMATION

A. Grid Convergence Study

We chose five different grid sizes, namely G1, G2, G3, G4 and G5, to ensure that the results obtained from the computations have been independent of grid resolution and implemented grid convergence index (GCI) method to test grid convergence. The computational domain has been discretized with unstructured triangular mesh elements with refinements along the walls and the interfaces for each of the four grid resolutions. However, in order to distinguish miniscule fluidic structures and track them without any numerical issues we used dynamic grid refinement in each direction. This refinement also ensured that the parasitic or spurious current for Re = 2000 and 4000 cases remains of the order of $10^{-5} - 10^{-4}$. The major differences between G1, G2, G3, G4 and G5 grid resolutions have been in the number of elements and the average (and minimum) quality of the elements, as shown in Table I.

Figure S1 (a) shows the variation of dimensionless drop ($i = 3$, liquid phase) volume ($D_{\mathrm{vol}} = 6D_{\mathrm{vol}}^{\mathrm{Actual}}/\pi {d_{\mathrm{d}}}^3$) whereas, plot S1 (b) shows the percentage relative error in the dimensionless drop volume calculation for the above-mentioned grid resolutions. Plot (b) shows that the percentage relative error in D_{vol} for G1 and G2 is around 2.99%, while for G2 and G3 grids the error is around 2.27%. For G3 and G4, the difference in D_{vol} reduces to 0.71%, whereas, for G4 and G5 it reduces to less than 0.2%. The analysis in Fig. S1 shows that the grid resolutions G3, G4, and G5 can be selected for the subsequent simulations for optimal computational time and without compromising the accuracy of the results.

Furthermore, to ensure minimal mass loss of liquid drop ($i = 3$) post-impact for the chosen grid resolutions G3, G4, and G5, we computed D_{vol} with dimensionless time (t) and plotted the same (along with % error) in Fig. S2 for highest Re and We cases. Figures S2 (a), (b), and (c) show the variation of with t for the grid resolutions G3, G4, and G5, respectively. Figure S2 (b) shows that, for a considerable amount of time ($t = 0 - 400$) during the computation, D_{vol} changes from 1 to ~ 0.994 (minimum ~ 0.99) ensuring the % error in calculation of D_{vol} does not exceed 1% at any given time (average $\sim 0.71\%$) for the grid resolution G4. Certainly, the results improve in case of G5 as shown in Fig. S2 (c), however, the improvements gained is this case comes at the expense of increased computational cost. Both the analysis presented in Figs. S1 and S2 together justify the selection of grid resolution G4 to save computational time without compromising on the accuracy for the rest of the numerical simulations.

Grid Resolution	Number of Mesh Elements	Minimum Mesh Quality	Average Mesh Quality
G1	0.923×10^5	0.70	0.92
G2	1.034×10^5	0.73	0.97
G3	2.025×10^5	0.74	0.98
G4	3.245×10^5	0.75	0.99
G5	5.276×10^5	0.78	0.99

TABLE I. Comparison of number of mesh elements and mesh quality for grid resolutions G1, G2, G3, G4 and G5.

* Corresponding Author; dipban@iitg.ac.in

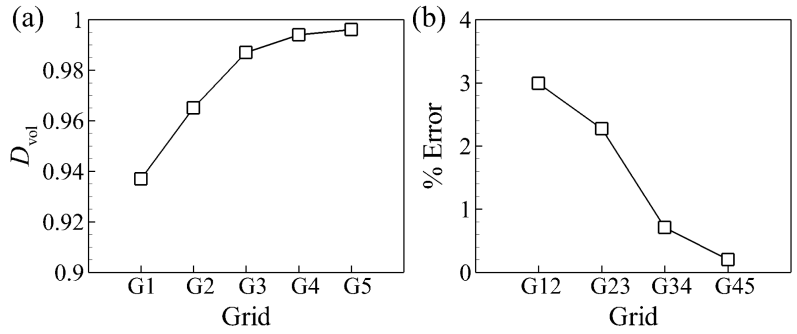

FIG. S1. Plot (a) shows the variation of dimensionless drop ($i = 3$) volume ($D_{\rm vol}$) for different grid resolutions. Plot (b) shows percentage relative error (Gij = parameter value at Gj relative to Gi, $i = 1 - 4$ and $j = 2 - 5$) using GCI method for the Re = 4000 case ($\eta_{\rm r} = 1$, $\sigma_{\rm r}^{12} = 12$, $\sigma_{\rm r}^{13} = 8$, We = 1600, Re = 4000, and Fr = 203.87).

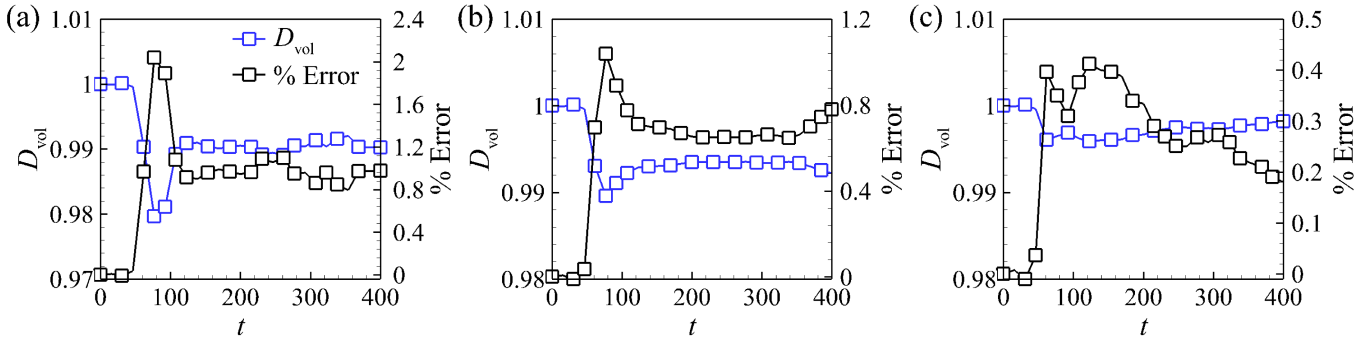

FIG. S2. Plots (a), (b), and (c) show the variation of dimensionless drop ($i = 3$) volume ($D_{\rm vol}$) (blue symbols, left side of the y-axis) and % error (black symbols, right side of the y-axis) with dimensionless time (t) for chosen grid resolutions G3, G4, and G5, respectively.

B. Model Validation – Bubble Entrainment

Previous studies have established that the gas bubbles of sufficient size rising through the stratified layers can entrain some volume of the denser fluid from the carrier layer into the target layer which is lighter in density [1, 2]. It has been shown that discrete gas bubbles must exceed a minimum volume to cause this type of entrainment experimentally and a corresponding theoretical criterion has been developed to predict this onset condition [2] This criterion implies that a bubble diameter greater than 5.52 mm can penetrate the interface between two stratified layers [1, 2]. The critical bubble diameter was also evaluated from the present numerical model in our earlier work [3]. In that study, the critical bubble diameter is predicted to be ~ 5.8 mm, which satisfies well with the criterion set by Greene *et al.* [1, 2]. The phenomenon of liquid entrainment while the bubble continues to rise through a set of stratified layers of fluids was validated with the theoretical, numerical and experimental results of Boyer *et al.* [4], Greene *et al.* [1, 2] and Bonhomme *et al.* [5] both qualitatively and quantitatively in our earlier paper which also employed the same numerical model [3].

C. Model Validation – Droplet Impact

In order to further validate the numerical approach employed in the present work, we have also compared the results of ternary phase drop impacts with the recent experimental studies of Jain *et al.* [6]. The details of which are elaborated in the subsequent figures. The setup of the numerical model in this case is similar to the schematic diagram shown in Fig. 1 of the main manuscript.

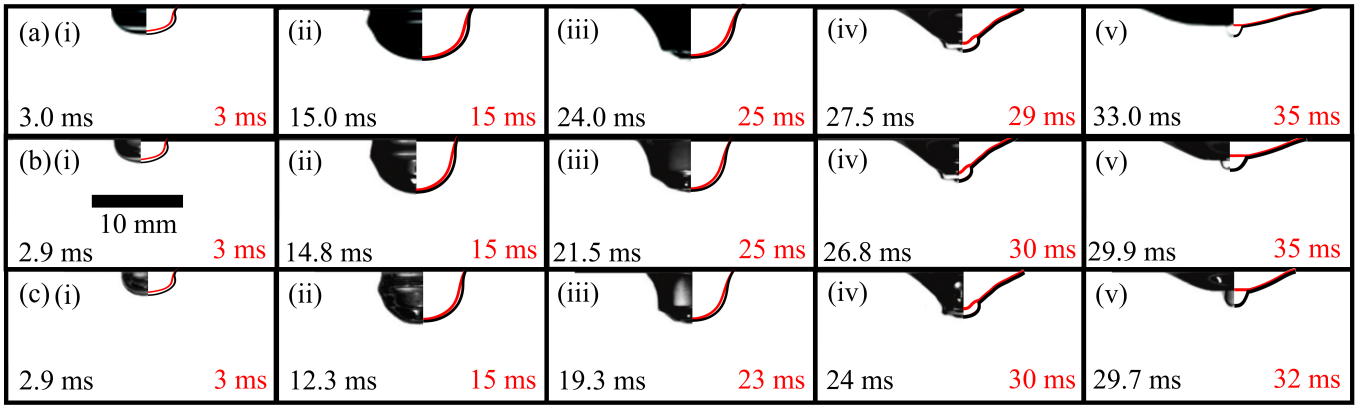

FIG. S3. Images (i) – (v) show the spatiotemporal evolution of the sub-surface events after the deep-pool water impact of (a) 35 cSt silicone oil drop with Fr = 178, We = 841, Re = 220, corresponding to Ca = 3.82, (b) 50 cSt silicone oil drop with Fr = 187, We = 868, Re = 156, corresponding to Ca = 5.56, and (c) 100 cSt silicone oil drop with Fr = 172, We = 822, Re = 76, corresponding to Ca = 10.81. The left pane (Grayscale) in each image correspond to the experimental results of Jain *et al.* [6], whereas, the right pane in each image shows the results from the present numerical study. The red, black, and red-black lines indicate the air-oil, water-oil, and air-water interfaces in a 2-D plane, respectively. The experimental (black) and the numerical (red) time scales are shown in each image panel.

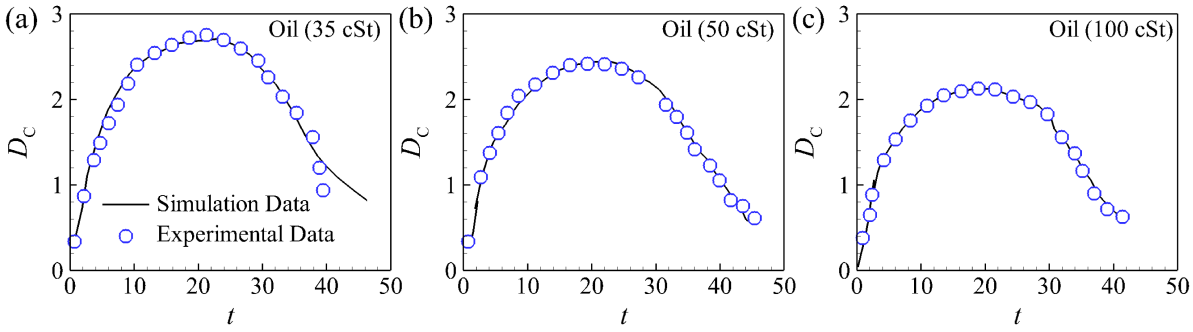

FIG. S4. A comparison of dimensionless crater depths (D_C) with dimensionless time (t) of experimentally determined data with those obtained from present numerical simulations [6]. Only 1 in 4 experimental data points are shown for clarity. Impact of (a) 35 cSt silicone oil drop with Fr = 178, We = 841, Re = 220, corresponding to Ca = 3.82, (b) 50 cSt silicone oil drop with Fr = 187, We = 868, Re = 156, corresponding to Ca = 5.56, and (c) 100 cSt silicone oil drop with Fr = 172, We = 822, Re = 76, corresponding to Ca = 10.81.

1. *Qualitative Comparison*

Qualitatively, the present numerical model has been validated with the experimental results of Jain *et al.* [6], the results of which is shown pictorially in Fig. S3. The results from the present numerical approach shows excellent agreement with the experimental results of Jain *et al.* [6] for a variety of the silicone oil drop impact having different viscosities. The time scales also match well within the permissible limits. However, small discrepancies in the time scales are probably appearing because of the 2D axisymmetric numerical model used in the present study which does not exactly match the three-dimensional experimental setup of Jain *et al.* [6].

The present numerical model is also capable to qualitatively predict the similar spatio-temporal dynamics immediately after the deep-pool water impact of PP1 liquid drop with the experimental results of Yang *et al.* [7] as shown in our earlier paper [1]. However, it could not predict the curvature induced Rayleigh breakup of the PP1 drop at a later timescale as reported in the study of Yang *et al.* [7] This can be attributed to the 2D axisymmetric nature of the present numerical model which considers the azimuthal curvature to be constant. Furthermore, in the experiments the post-impact shape of the PP1 droplet does not remain symmetric along the axis of symmetry which is necessary prerequisite for the 2D axisymmetric models. These off-axis breakup aspects predicted by the experiments of Yang *et al.* [7] can be accurately predicted by employing a more comprehensive 3D numerical model based on the present 2D axisymmetric model which can be explored in future research.

2. Quantitative Comparison

Quantitatively, the experimental data of Jain *et al.* [6] related to the crater depth with the variation in time are compared with the numerical data points from the present study in Fig. S4. The plots (a), (b), and (c) in Fig. S4 show that the crater depth dynamics matches quite well with the experimental observations [6]. Only the decay dynamics of the crater in case of plot (a) shows a marginal deviation from the experimental data obtained in the previous study.

D. Energy Analysis of Different Types of Drop Impact

Figures 8 − 10 highlight that the dimensionless crater depth ($D_{\rm C}$) monotonically increases to a local maximum with increasing dimensionless time (t) after initial impact of the drop. The growth of the crater with time can be evaluated analytically considering a hemispherical crater in potential flow [8]. Assuming a hemispherical crater, Liow used the drop impact as the source of energy and obtained the kinetic energy of the crater as [9],

$$E_K^C = -\frac{\rho_2}{2}\int\int \Xi \frac{\partial \Xi}{\partial r} dS = \pi \rho_2 D_{\rm C}^3 \left(\frac{dD_{\rm C}}{dt}\right)^2, \tag{S1}$$

where, $\Xi = \dfrac{D_{\rm C}^2}{r}\dfrac{dD_{\rm C}}{dt}$ is the velocity potential, ρ_2 is the density of the water and S is the surface element.

In order to obtain a scaling for the maximum cavity depth, the total energy available for the cavity growth process is assumed to be supplied by the kinetic energy of the drop ($E_K^D = \pi \rho_3 d_{\rm d}^3 u^2/12$) entirely. However, Figs. 7 (c) and (d) show that immediately after the drop impact irrespective of the shape of the droplet the kinetic energy of the droplet reduces by $\sim 75\%$, which means that due to the impact almost 75% of the initial kinetic energy of the droplet is lost in the surroundings in the form either heat, sound, viscous or other forms of energy dissipations. Therefore, remaining 25% of the initial kinetic energy of the droplet is responsible for the crater's evolution as well as new creation of surfaces apart from the viscous dissipation in the water pool. The potential energy of the cavity (E_P^C) formed can be expressed as $E_P^C = \pi \rho_2 g D_{\rm C}^4/4$. The total energy balance can be obtained by converting the remaining kinetic energy of the impacting drop ($\frac{1}{4}E_K^D$) to the kinetic energy of the crater evolution (E_K^C), gravitational potential energy (E_P^C), viscous dissipation energy (E_V), and the surface energy (E_S) due to the creation of additional surface area of the crater, which can be expressed as [3, 9],

$$E_K^C + E_P^C + E_V + E_S = \frac{1}{4}E_K^D. \tag{S2}$$

In the differential form the same expression can be rewritten as,

$$\pi \rho_2 D_{\rm C}^3 \left(\frac{dD_{\rm C}}{dt}\right)^2 + \frac{1}{4}\pi \rho_2 g D_{\rm C}^4 + 8\pi \eta_2 \int D_{\rm C}\left(\frac{dD_{\rm C}}{dt}\right)^2 dt + \left(\sigma_{13} + \sigma_{23} - \sigma_{12}\right) A_{\rm S} = \frac{\pi \rho_3 d_{\rm d}^3 u^2}{48}. \tag{S3}$$

Here, the first term in the left-hand side denotes E_K^C, the second term denotes E_P^C, the third term signifies E_V, and the fourth term represents E_S. It is important to note here that, viscous dissipation energy (E_V) is small compared to the kinetic energy of the drop which can be represented by $1/{\rm Re} = O\left(10^{-3}\right)$ and thus can be neglected in Eq. (S3). Also, the notation, $A_{\rm S}$ in the fourth term signifies the maximal area covered by the drop onto the crater surface. A few recent theoretical studies have shown a similar type of energy balance for a drop impact problem in case of binary liquids; however, these formulations neglected the contribution of one or more energy components in the overall energy balance [3]. The present analysis initially incorporates all four possible energy terms in Eq. (S3) and simplify the formulation later on based on the order of magnitude analysis. We have also shown a similar type of energy analysis in our earlier paper considering only spherical shape of the droplets, however, in the present analysis we incorporated the subtleties of the initial shape of the droplet into the theoretical framework [3].

The area of maximum spreading ($A_{\rm S}$) over the crater at the maximum crater depth can be measured for all the different prolate and oblate droplet impacts from the numerical simulations. Figure S5 shows the variation of $A_{\rm S}$ normalized by the equivalent cross-sectional area of the impacting drop, $A_0 = \pi d_{\rm d}^2/4$ with the change in We for the different cases. Plots (a) and (b) of Fig. S5 illustrate that, $A_{\rm S}$ increases proportionally with the change in We, which can be mathematically expressed as, $(A_{\rm S}/A_0) - 1 \propto {\rm We}$ for both prolate and oblate droplet impacts. Therefore, the expression can be further correlated as, $A_{\rm S} = A_0\left(1 + N{\rm We}\right) = \left(\pi d_{\rm d}^2/4\right)\left(1 + N{\rm We}\right)$, where, N is the proportionality constant and can be obtained from the slope of the fitted lines (black continuous line) in Fig. S5 (a) and (b). This

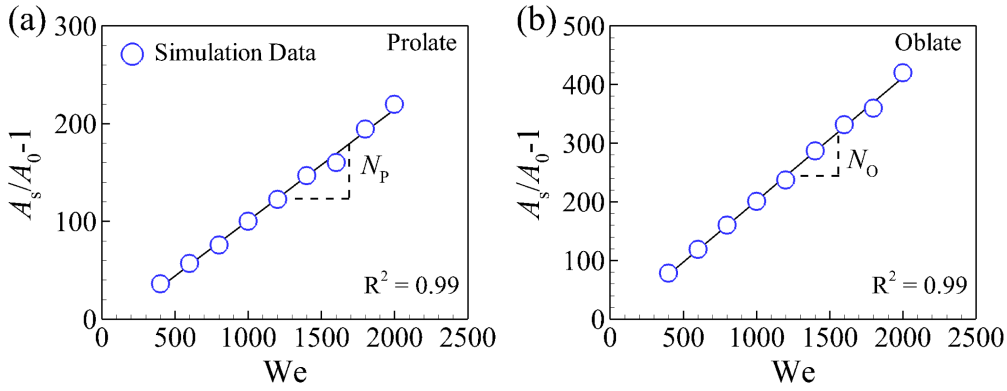

FIG. S5. Plots (a) and (b) show the variation of normalized area of spreading ($A_S/A_0 - 1$) with increasing We for prolate and oblate droplet impacts, respectively. The other parameters used in these results are same as mentioned in Figs. 2 and 4 of the manuscript.

measurement from the simulations matches closely with the experimental observations of Lhuissier *et al.* [10]. The fitted lines (black continuous lines) in Fig. S5 (a) and (b) also indicate that the proportionality constant (N) or the slope of the line is different for prolate ($N_P = 0.11$) and oblate ($N_O = 0.21$) shape of the initial droplet. It is important to note that, the slope (N_P and N_O) also determines that how much surface energy is generated after the impact, because, E_S ($\propto A_0\,[1 + N\mathrm{We}]$) is directly proportional to the slope of the fitted line. So, the amount of initial kinetic energy of the droplet which is getting converted into the surface energy for prolate droplet impact is comparatively less than that of an oblate droplet impact, because, $N_P < N_O$.

Rearranging Eq. (S3), we obtain the following expression,

$$\frac{48\rho_2 D_C^3}{\rho_3 d_d^3 u^2}\left(\frac{dD_C}{dt}\right)^2 + \frac{12\rho_2 g D_C^4}{\rho_3 d_d^3 u^2} + \frac{12\Delta_3\,(1 + N\mathrm{We})}{\rho_3 d_d u^2} = 1. \tag{S4}$$

Here, the first term defines the fraction of the initial kinetic energy of the drop that is converted to kinetic energy of the crater ($E_K = E_K^C/E_K^D$), the second term denotes the ratio of gravitational potential energy and initial kinetic energy of the drop ($E_P = E_P^C/E_K^D$), and the third term denotes the fraction of initial kinetic energy of the drop which is converted to surface energy ($E_I = E_S/E_K^D$). The coefficient, $S_3 = -\Delta_3 = (\sigma_{12} - \sigma_{13} - \sigma_{23})$, is termed as spreading coefficient of the phase $i = 3$ (oil) at the interface between phases $i = 1$ (air) and $i = 2$ (water). Non-dimensionalization of Eq. (S4) results in the following expression,

$$\left(\frac{48}{\rho_r}\right) D_C^3 \left(\frac{dD_C}{dt}\right)^2 = 1 - \left(\frac{12}{\rho_r}\right)\left(\frac{1}{\mathrm{We}} + N\right)\left(\sigma_r^{13} + 1 - \sigma_r^{12}\right) - \left(\frac{12}{\rho_r}\right)\left(\frac{D_C^4}{\mathrm{Fr}}\right). \tag{S5}$$

The numerical analysis in the present study deals with droplet impacts where, Fr is large, $\mathrm{Fr} \sim O\left(10^2\right) - O\left(10^3\right)$, then the last term in the right-hand side of the expression in Eq. (S5) can be neglected. This neglected term essentially signifies the energy ratio E_P.

If we integrate the expression from Eq. (S5) we obtain the following expression after rearrangement,

$$\int_0^{D_{Cm}} \sqrt{\frac{(48/\rho_r)\,D_C^3}{\left[1 - \left(\frac{12}{\rho_r}\right)\left(\frac{1}{\mathrm{We}} + N\right)\left(\sigma_r^{13} + 1 - \sigma_r^{12}\right)\right]}}\, dD_C = \int_0^{t_m} dt. \tag{S6}$$

Considering, $E_R = \left(\frac{12}{\rho_r}\right)\left(\frac{1}{\mathrm{We}} + N\right)\left(\sigma_r^{13} + 1 - \sigma_r^{12}\right)$ and $\rho_r = 1$, the Eq. (S6) reduces to,

$$\frac{D_{Cm}^5}{t_m^2} = \frac{1 - E_R}{7.68}. \tag{S7}$$

The dimensionless term, E_R in Eq. (S7) signifies the ratio between the surface energy and the initial kinetic energy of the drop (E_I) in the dimensionless form. Therefore, E_R provides the quantification of the percentage of initial kinetic energy getting converted to create the new interfaces after the drop impact. Mathematically, the quantity E_R

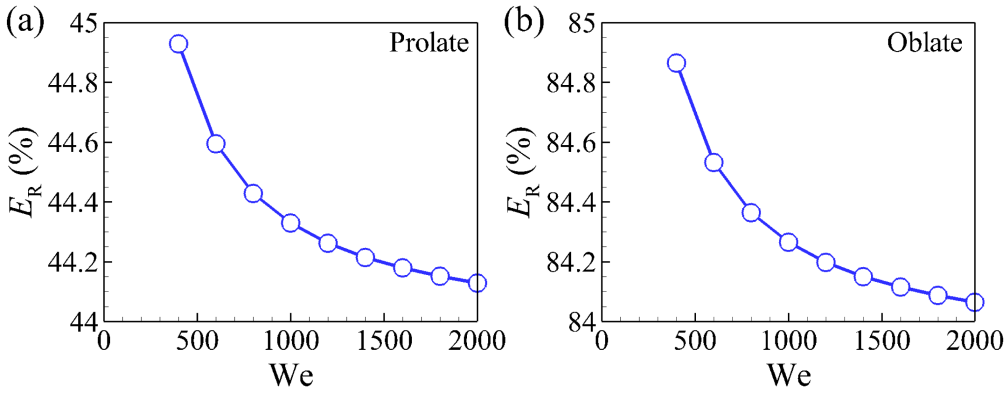

FIG. S6. Plots (a) and (b) show the variation of energy conversion ratio ($E_{\rm R}$) with increasing We for prolate and oblate droplet impacts, respectively. The other parameters used in these results are same as mentioned in Figs. 2 and 4 of the manuscript.

in Eq. (S7) depends on the pre-impact shape of the droplet because the term N in the expression of $E_{\rm R}$ is different for prolate ($N_{\rm P}$) and oblate ($N_{\rm O}$) shape of the droplet.

Plots (a) and (b) in Fig. S6 show the variation of energy conversion ratio ($E_{\rm R}$) with the increase in We for prolate and oblate drops respectively. Figure S6 also shows that for a given We, the energy conversion in case of an oblate droplet impact is almost two times higher than the droplet impact with a prolate shape. This quantification matches well with the observation in Fig. S5, since, $E_{\rm R} \propto N$, and $N_{\rm O}$ is almost two times higher than $N_{\rm P}$. This signifies that the majority of the kinetic energy ($\sim 84-85\%$) supplied by the drop impact is converted to the surface energy in case of a oblate drop impact. Therefore, the amount of kinetic and potential energy left for the crater to undulate with is less ($\sim 15-16\%$) in case of an oblate drop impact. This is the reason behind the drastic reduction in the interface velocity (or kinetic energy of the crater) in case of oblate droplet impact as shown in Figs. 7(c) and 7(d). Furthermore, due to the low conversion of the kinetic energy to surface energy ($\sim 44-45\%$) in case of a prolate drop impact, the rest of the energy ($\sim 55-56\%$) gets transferred to the newly formed flow structures inside the liquid pool as a kinetic energy. This extra kinetic energy received by the new flow structures such as, oil-toroid, and the entrapped drop due to the impact pushes the flow structures towards the downward direction long after the impact. This phenomenon is already described during the analysis of Figs. $2-5$ of the manuscript.

Employing the values of $N_{\rm P}$ ($=0.11$) and $N_{\rm O}$ ($=0.21$) from the Fig. S5 and the other parameters from the numerical simulations into the expression of $E_{\rm R}$, and simplifying Eq. (S7) for prolate and oblate droplet impacts, we get the following expressions for the crater dynamics for different types of drop impacts,
(i) for prolate droplets,

$$D_t = \frac{D_{\rm Cm}^5}{t_{\rm m}^2} = 0.1016 - 0.26\left(\frac{1}{\rm We}\right), \tag{S8}$$

and (ii) for oblate droplets,

$$D_t = \frac{D_{\rm Cm}^5}{t_{\rm m}^2} = 0.0756 - 0.26\left(\frac{1}{\rm We}\right). \tag{S9}$$

The energy analysis from our earlier paper reveals that for spherical droplet impacts the same can be expressed as [3],

$$D_t = \frac{D_{\rm Cm}^5}{t_{\rm m}^2} = 0.365 - 1.03\left(\frac{1}{\rm We}\right). \tag{S10}$$

[1] G. A. Greene, J. C. Chen, and M. T. Conlin, Int. J. Heat Mass Transf. **31**, 1309 (1988).
[2] G. A. Greene, J. C. Chen, and M. T. Conlin, Int. J. Heat Mass Transf. **34**, 149 (1991).
[3] J. Chaudhuri, T. K. Mandal, and D. Bandyopadhyay, Phys. Fluids **34**, 012011 (2022).
[4] F. Boyer, C. Lapuerta, S. Minjeaud, B. Piar, and M. Quintard, Trans. Porous Med. **82**, 463 (2010).

[5] R. Bonhomme, J. Magnaudet, F. Duval, and B. Piar, J. Fluid Mech. **707**, 405 (2012).
[6] U. Jain, M. Jalaal, D. Lohse, and D. van der Meer, Soft Matter **15**, 4629 (2019).
[7] Z. Q. Yang, Y. S. Tian, and S. T. Thoroddsen, J. Fluid Mech. **904** (2020).
[8] O. G. Engel, J. Appl. Phys. **37**, 1798 (1966).
[9] L. J. Leng, J. Fluid Mech. **427**, 73 (2001).
[10] H. Lhuissier, C. Sun, A. Prosperetti, and D. Lohse, Phys. Rev. Lett. **110**, 264503 (2013).